RESEARCH

Open Access

Designing and additive manufacturing of talus implant for post-traumatic talus avascular necrosis: a case study

François Antounian[1], Hayk Avagyan[2], Tsovinar Ghaltaghchyan[3], Yaroslav Holovenko[4], Hayk Khachatryan[1] and Marina Aghayan[3*]

Abstract

New technologies in additive manufacturing and patient-specific CT-based custom implant designs make it possible for previously unimaginable salvage and limb-sparing operations a practical reality. This study presents the design and fabrication of a lattice-structured implant for talus replacement surgery. Our primary case involved a young adult patient who had sustained severe damage to the talus, resulting in avascular necrosis and subsequent bone collapse. This condition caused persistent and debilitating pain, leading the medical team to consider amputation of the left foot at the ankle level as a last resort. Instead, we proposed a Ti6Al4V-based patient-specific implant with lattice structure specifically designed for pan-talar fusion. Finite element simulation is conducted to estimate its performance. To ensure its mechanical integrity, uniaxial compression experiments were conducted. The implant was produced using selective laser melting technology, which allowed for precise and accurate construction of the unique lattice structure. The patient underwent regular monitoring for a period of 24 months. At 2-years follow-up the patient successfully returned to activities without complication. The patient's functional status was improved, limb shortening was minimized.

Keywords Talus implant, Additive manufacturing, Customized implant, Simulation

Introduction

Today, numerous biomedical applications employ personalized products, such as prosthetics and implants that replace injured limbs or bones, whether partially or completely [1, 2]. Patient-specific metallic orthopedic implants manufactured using additive manufacturing (AM) have garnered significant attention due to their accelerated bone regeneration effects [3, 4]. Importantly,

AM enables the creation of implants with high geometrical freedom, accuracy and precision using initial data from medical images [5–7].

Recently, AM technology is used to produce metal- and ceramic-based implants for total talar replacements (TTR), which give promising outcomes at early-or mid-term follow up reports [6, 8]. The complication rate is still high at long-term follow-up [6]. Reports mainly addressed TTR with smooth metallic or ceramic implantation, which give promising outcomes in early- and mid-term follow-up [9, 10]. However, high complication rates are registered in long term follow-up [11, 12]. Morita et al. showed long-term results after using alumina ceramic based implants [13]. They achieved significant improvement in pain and function. Similar implants were chosen

*Correspondence:
Marina Aghayan
marina.aghayan@ichph.sci.am
[1]AIP Tech CJSC, 5/2 Paruyr Sevak, Yerevan 0619, Armenia
[2]WIGMORE CLINIC CJSC, Yerevan, Armenia
[3]A.B. Nalbandyan Institute of Chemical Physics NAS RA, Yerevan, Armenia
[4]3D Metal Tech LLC, Kyiv, Ukraine

by Katsui et al. [14]. After 12–84 months follow-up they concluded that the alumina based custom whole -talus implants are excellent for patients with comminuted talar fractures. However, results are not good for open fracture and bony defects. Alumina-based ceramic prostheses indeed show promising results, but they are costly and time-consuming to produce [6].

Abramson et al. reported about 8 patients who underwent TTR using titanium based bulk implants with smooth surface [11]. After the follow up period (range 12–49 months) the mean American Orthopedic Foot and Ankle Society (AOFAS) score was 79.25 (range, 69–88). The patient with the longest duration of follow-up showed radiological changes of tibial wear, although he remained symptom free. Kadakia et al. reported about 27 patients at a follow-up range of 12–43 months using cobalt-chromium TTR implants [15]. There were three complications. The outcome scoring using the Foot and Ankle outcome score (FAOS) for the patient improved significantly.

Dekker et al. used titanium cage for complex foot and ankle limb salvage, deformity correction, and arthrodesis procedures [16]. They noticed bone incorporation in 13 of 15 patients. Two patients had failure because of infection and nonunion. The authors proposed that when titanium implants are used, there is a risk of infection, particularly in uncontrolled diabetic patients and smokers. Abar et al. [17] reported about 39 cases with 12–74 months follow-up using 3D printed titanium cages. Thirteen cases required additional surgery, of which three were because of failure of non-3D printed hardware, ten implants were removed because of nonunion. Ramhamadany et al. used titanium cages for three patients [18]. During follow-up period (range 24–48 months) no postoperative complications were recorded. Each patient progressed to satisfactory union with bridging trabeculae and incorporation of bone into the cage structure by 1 year.

The aim of our work is to design and manufacturing of a patient-specific orthopedic implant for talus replacement with a lattice structure for treatment of defect created because of the death and collapse of the talus Avascular necrosis (AVN).

Lattice structures offer several advantages, including stiffness fine-tuning, weight control through lightweight design, osteoconductivity, and osteointegration [19–23]. Consequently, extensive efforts have been devoted to understanding the properties of lattice structures and their advantages or limitations for specific applications [24–26].

The predominant metals used in implants have much higher modulus and strength creating a stress-shielding effect. For example, Ti-based alloys have Young's modulus and ultimate tensile strength of 105–125 GPa and 758–1200 MPa, respectively. Creating a lattice structure may reduce the effective modulus and help avoid stress-shielding effects. At the same time, lattice structure provides additional benefits, i.e. weight reduction of the implants. The main challenge of lattice structures is to maintain mesh strength in all directions. Lattice structures can thus be very robust against compression but break relatively easily when twisted.

Experimental

Design of the customized implants

Digital model of the implant is created based on imaging data obtained from the damaged area. The commonly employed techniques for capturing and imaging are "thin slice" Computed Tomography (CT) or Magnetic Resonance Imaging (MRI).

In order to generate Computer-Aided Design (CAD) models for CT raw data, we used the Materialise Mimics 22.0 imaging software. Volume rendering was done followed by surface rendering (high resolution and pixel value 200). The file was then exported to STL format, in order to compare CT-data with 3D surface scan data. (Fig. 1)

After creating the implant model, a finite element simulation is conducted to estimate its performance. COMSOL Multiphasic software package was used for Finite Element Method (FEM) simulation. The implant model was imported into COMSOL Multiphysics software, and a solid object with defined material properties was generated. A linear elastic material model was assigned to the mesh material, with Young's modulus and Poisson's ratio values obtained from the software database. The size of mesh and number of degrees of freedom, as well as, parameters of mesh, boundary conditions, boundary and loading conditions is detailed in Additional file 1.

The simulation results serve as a basis for fine-tuning and optimizing the model to meet specific requirements. Figure 1 (c-d) depicts the implant model based on CT data for talus replacement.

To evaluate the mechanical behavior of the mesh structure, a numerical simulation was performed using COMSOL Multiphysics software (version 5.0, COMSOL Inc., Burlington, MA, USA). The software's capabilities in finite element analysis were utilized to model and simulate the mesh structure under various loading conditions.

The mesh geometry was imported into COMSOL Multiphysics, and a three-dimensional model was created. The mesh structure was considered a solid object with defined material properties. A linear elastic material model was assigned to the mesh material. Young's modulus and Poisson's ratio values was obtained from the software database.
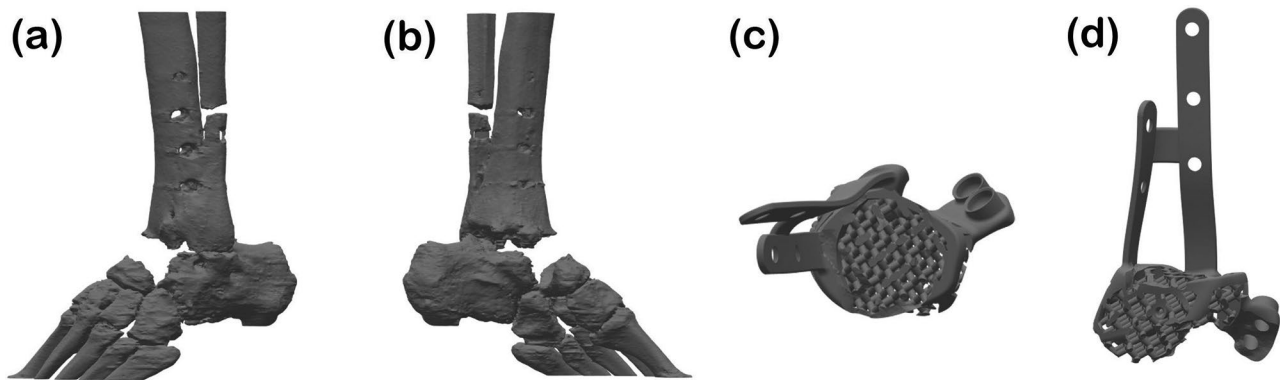
Fig. 1 (**a-b**) Model of the bone, (**c-d**) model of the implant. CT data was used to generate the CAD model of the bone. The implant model was created to fill the void of the bone defect

The simulation involved application of mechanical loads to the mesh structure to analyze its deformation and stress distribution. Boundary conditions, including fixed supports and applied loads, were defined based on the experimental setup. The simulation was performed using a stationary solver with appropriate settings to accurately capture the mesh's response.

The mesh structure was discretized using a suitable meshing technique provided by the software. A combination of tetrahedral and other element types was employed to accurately represent the geometry and capture the behavior of the mesh structure.

It is important to note that the simulations were conducted under idealized conditions, assuming linear elastic behavior and neglecting potential non-linear effects. The simulations served as a complementary tool to the experimental investigation, providing insights into the mesh structure's mechanical response and aiding in the interpretation of the experimental findings.

Compressive testing

Compressive testing of the specimens was conducted using an Instron 5100 Universal Testing Machine (Instron Corporation, Norwood, MA, USA). The samples were subjected to a constant loading rate of 5 mm/min, which was applied using the crosshead displacement control mode of the Instron 5100 machine. This loading rate was selected based on prior research to ensure a consistent and controlled deformation rate across all tested specimens [27]. Two types of geometry were explored, (i) cubic and (ii) cylindrical structure to ensure reliability. The cubic samples were $19 \times 19 \times 19$ mm in size while the cylindrical samples were 18 mm in diameter and 27 mm in height. Applied force was up to 5100 N to estimate the cracking onset [27]. Using high load, it was possible to estimate the points of critical failures and crack generation. Thus, in some samples a high load was applied aiming to monitor the crack formation and propagation process.

The compressive testing was conducted until the desired strain or a predefined endpoint was reached. The force-displacement data were continuously recorded by the Instron Bluehill® software. To ensure the repeatability and reliability of the experimental results, a minimum of three replicate tests were performed for each specimen configuration.

Additive manufacturing

Gas atomized Ti-6Al-4 V Grade 23 (AP&C, Canada) powder with a particle size of 15–45 μm was used. The samples and talus implants were fabricated using Concept Laser M2 machine, at a scanning speed of 900 mm/s, laser power of 80 W, spot size of 50 μm, layer thickness of 25 μm. Layers were scanned by continuous laser in stripped pattern, which was rotated 60° between each layer. Argon was employed as a protective gas, and the oxygen content was kept below 0.05% during the manufacturing process. The platform pre-heating temperature was maintained at 200 °C.

All samples and the talus implant were annealed at 750 °C for 4 h, at heating rate of 5 °/min in a furnace under argon atmosphere, then were gradually cooled to room temperature. The samples were cleaned in bath ultrasound in ethyl alcohol.

Results and discussion
The structure design, simulation and mechanical testing
The mesh structure of the talus implant was designed using periodically repeated unit cells. Numerous mesh structures have been studied and verified in the literature, demonstrating that the structure, shape, and unit cell size significantly contribute to the mechanical performance of customized implants [28, 29]. Considering the specific requirements for the talus implant, such as low weight, sufficient load-bearing capacity (approximately 100 kg), and large cell size to accommodate a bone graft, the unit cell size was set to be 10 mm.

In this study, we considered two different unit cell structures for the talus implant: (i) the "rotating cross" structure (Fig. 2), (ii) the "rhombic dodecahedron" structure (Fig. 3). The relative density of all unit cells was set to 30%.

To assess the performance of this lattice structure, a load of 100 kg (approximately 980 N) was applied, representing the weight of a patient. Considering the surface area of the talus (approximately 0.002 m²) and load distribution between both feet, the load applied to the mesh structure for talus loading was approximately 73.5 kN/m².

Simulation results indicated that for "Rotating Cross" lattice structure stress concentration occurred when the load was applied in directions other than the normal direction (Fig. 2). Stress reached up to 25 MPa at the edges of the nodes where struts are connected, while normal loading resulted in stresses less than 2.8 MPa. It means shearing or twisting (e.g., loading at 45°) may lead to a fatal outcome. For the "Rhombic Dodecahedron" lattice structure, the loading direction has minimal effect (Fig. 3).

To verify the lattice structure's tolerance to mechanical loading, samples were tested in a universal testing machine. In Fig. 4 the applied force vs. strain (blue curve) and generated stress vs. strain (orange curve) are depicted for the "Rotating Cross" sample with a size of 19×19×19 mm. As Fig. 4 clearly shows the sample was
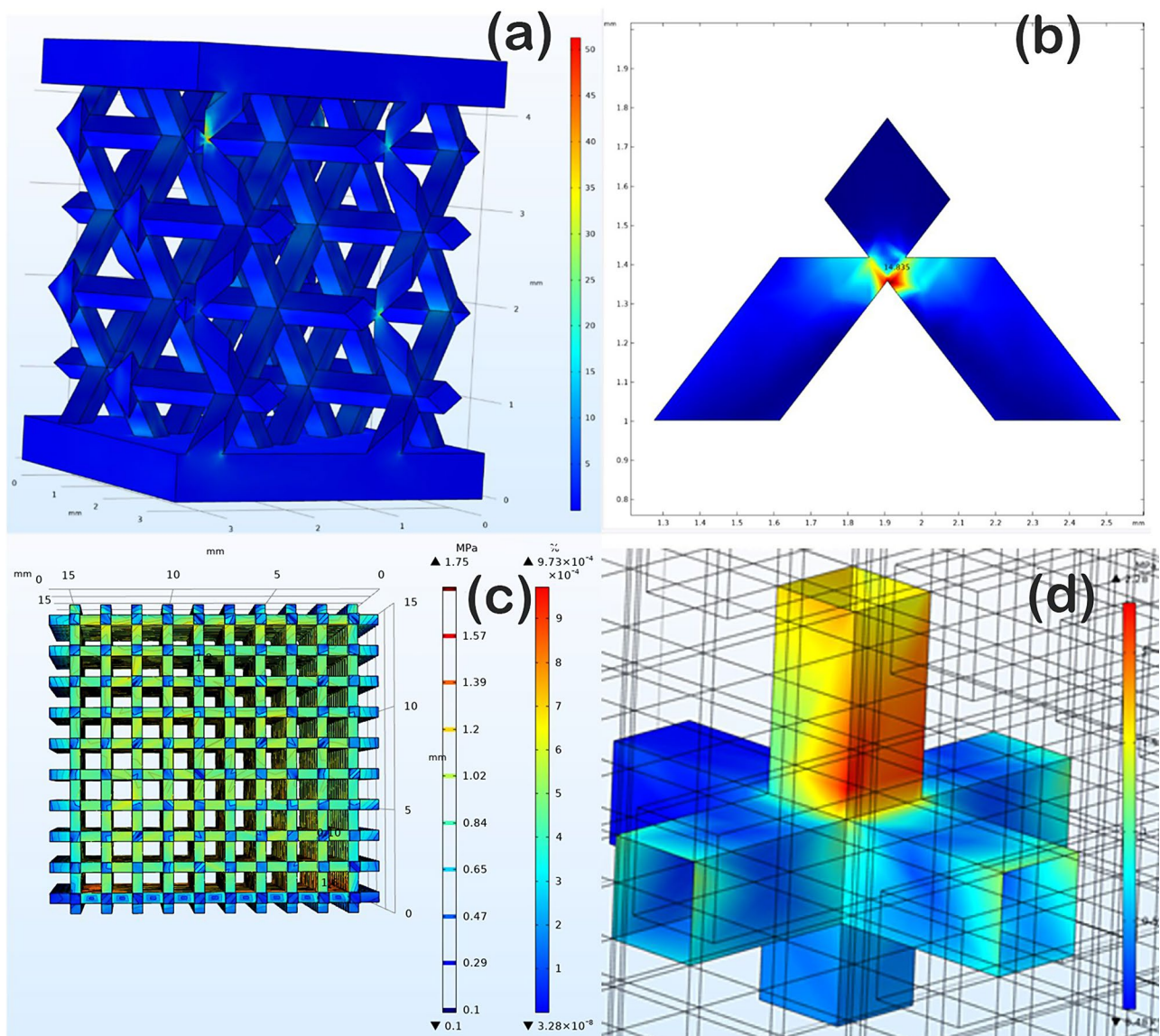

Fig. 2 Simulated results for the "Rotating Cross" lattice structure. The figure illustrates overall view of the 45° loaded samples (**a**), where stress reached to 25 MPa at the edges of nodes (**b**). The overall view of the samples loaded in the normal direction (**c**) shows that stress reaches to 2.28 MPa at the struts (**d**)
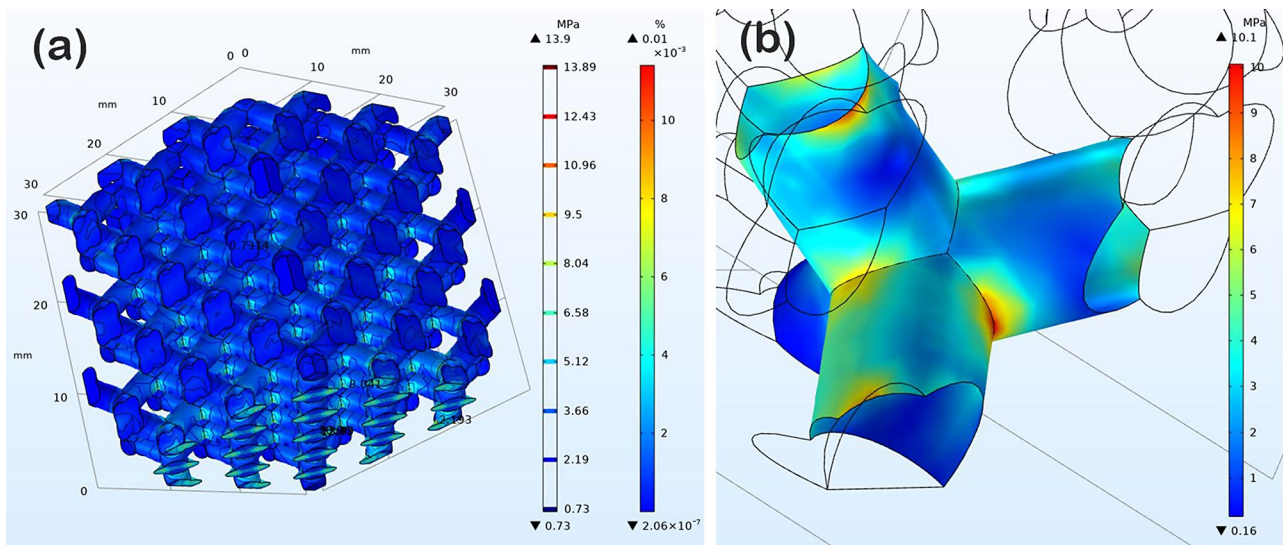
Fig. 3 Simulated results for the "Rhombic Dodecahedron" lattice structure. The figure illustrated overall view of the samples loaded in the normal direction (**a**), where stress reached to 10.1 MPa at nodes where struts are connected (**b**)
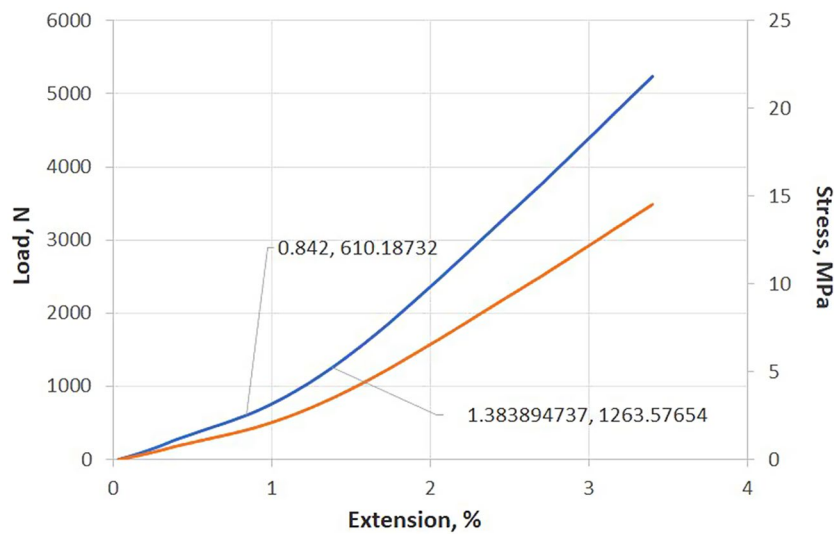

Fig. 4 Stress-strain curve and loading path for a cubic sample with the "Rotating Cross" structure. The blue curve illustrates applied force vs. strain, while orange curve shows the generated stress vs. strain

compressed up to 3.5% without fracture; however, plastic deformation occurred around 0.7–1.5%, indicated by a distinct transition zone in the stress-strain curve.

After three cycles of loading and unloading, the samples failed (Fig. 4). The failure may be attributed to the small rod dimensions during the printing process and stress concentrations at the strut connections.

In conclusion, even though the stress is well below the yield point of the Ti alloy, the sample failed to pass the fatigue test. This may be related to both poor printing processes due to small rod dimensions and stress concentrations at the strut connections. Both factors are important, hence we need to evaluate which one has the greater impact.

Figure 5 shows the SS curves and load hysteresis for a "rhombic dodecahedron" lattice (Fig. 5a) and dynamically loaded and unloaded sample response (Fig. 5b). Mechanical testing of the "Rhombic Dodecahedron" lattice structure demonstrated that the samples passed all tests without failures (Figs. 5 and 6). The hysteresis curve showed minimal energy dissipation, indicating that the sample withstood the load without undergoing mechanical changes.

The samples were then loaded at 5100 N and held for 1 h. After this loading cycle, the sample was dynamically cycled again, but the load was held relatively long.

As shown in Fig. 6, this multiple-loaded sample undergoes stress relaxation as the second cycle begins. A stress
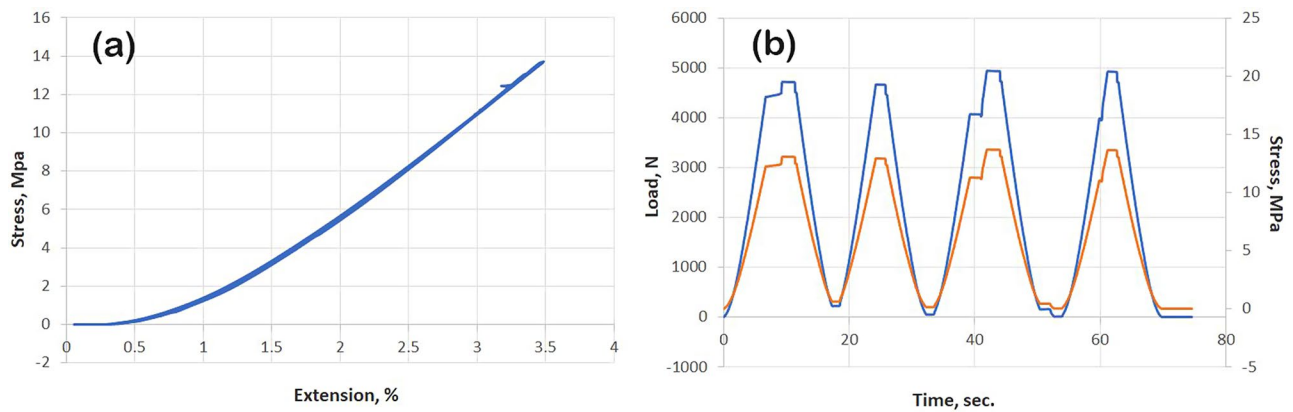
Fig. 5 SS curve and loading–unloading path for the cubic sample with "rhombic dodecahedron" structure. The samples withstand stress of 14MPa (**a**), and the cycled loading-unloading of load of 5100 N
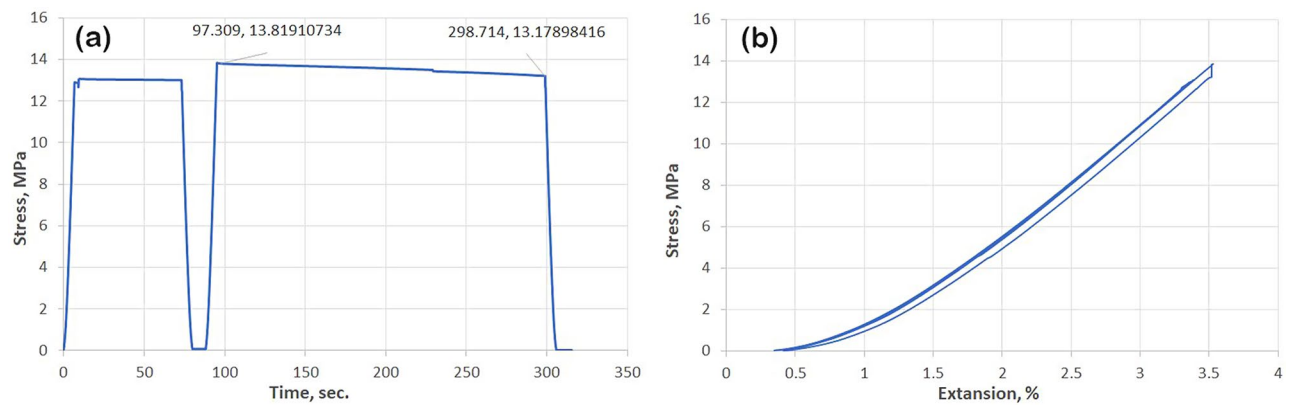

Fig. 6 Long-term loading – unloading path of "rhombic dodecahedron" cubic sample and hysteresis curve. Long-term loading – unloading path shows stress relaxation (**a**), which is evident in hysteresis of loading–unloading curve (**b**)
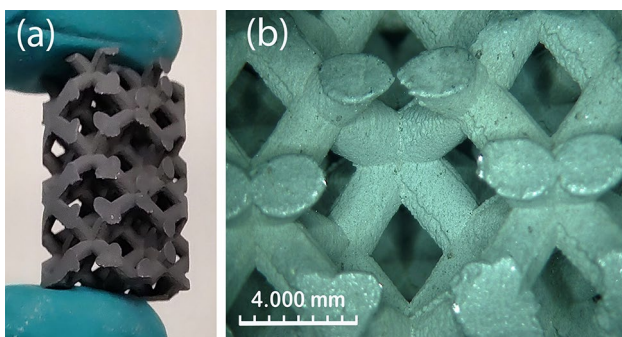

Fig. 7 Actual 3D printed lattice structure; (**a**) the view, and (**b**) its microstructure

of about 0.64 MPa was estimated to be released in 200 s. This change can be seen in the hysteresis curve where the unloading curve deviates from the load path.

These changes indicate that there have been specific changes to the sample. Further loading destroyed the sample (Fig. 6).

The modification of the lattice structure improved the mechanical performance, but the sample has not yet been qualified for use as an implant due to the risk of failure. The extreme load used in testing (5100 N) accelerated the failure and helped monitoring its mechanisms within a measurable time frame.

Further optimization was done by increasing the nodal diameter. Figure 7 shows the "rhombic dodecahedron" lattice structures with strut sizes of 2.5 mm. Both structures exhibit well-formed struts and none visible defects, unlike the thin node cases.

Figure 8a shows the SS curve of the "rhombic dodecahedron" sample loaded up to 5100 N. After loading, samples were held for 40 min and then dynamically loaded (Fig. 8b). Mechanical testing of the samples with increased strut sizes showed that they passed all tests without failures. This indicates that "rhombic dodecahedron" structures with strut sizes greater than 1.9 mm can be considered for implant design.

To explore the shear loading response, a 45° shear stress was applied to the samples. According to the results, the "rhombic dodecahedron" withstood all loads and no damage was found. This led to the conclusion that
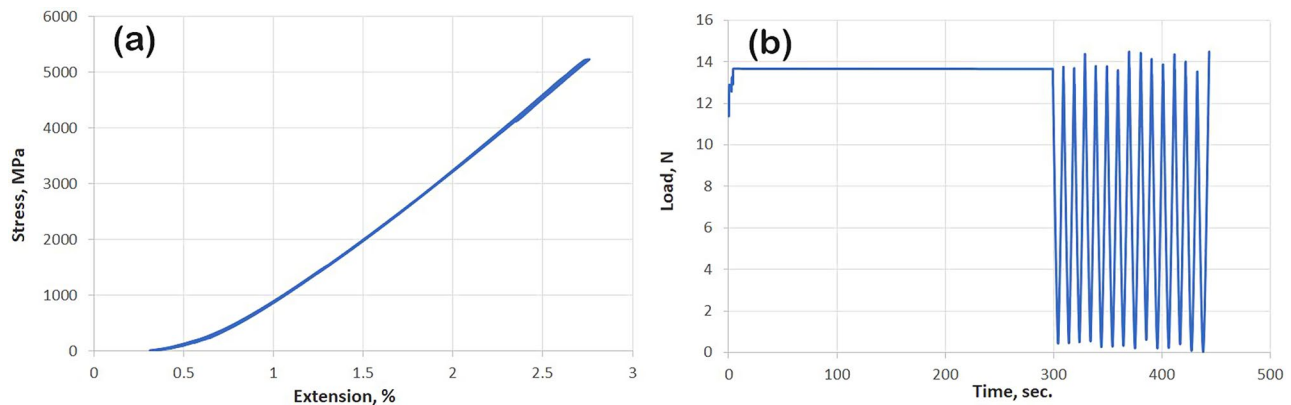
Fig. 8 SS curve of the "rhombic dodecahedron". (**a**) energy dissipation and (**b**) dynamic loading curves

the optimal structure of the talus might be the "rhombic dodecahedron".

Case description and treatment plan

The patient was a 41-year-old male surgeon who sustained a traumatic fracture dislocation of his left talus in 2016 in a car accident. He is a smoker and overweight with no other known medical comorbidities.

His initial treatment consisted of open reduction and internal fixation (ORIF) with screw fixation within 24 h, which failed to heal. This led to the removal of the screws a year post-surgery, and the nailing the ankle from the calcaneus up which ended with an established AVN of the talus.

In 2018, an attempt was made to fuse the ankle joint by a calcaneal-tibial locked nailing. In 2019, with no fusion visible on X-rays and with pain, he had drilling of the talus and tibia plus distal dynamization of the rod by removing the calcaneus screws.

This did not lead to fusion. There was increasing and disabling pain, a stiff ankle and subtalar joint with deformity in the midfoot. Advice was given to obtain a Syme amputation. He refused that option and sought advice on a salvage procedure.

His surgeon consulted us for a foot-sparing solution to rid the patient of pain and allow ambulation without crutches. The plan was not to gain ankle motion but to ambulate without pain retaining his foot. The solution of a pan-talar fusion with triple arthrodesis was proposed and accepted by the patient. The patient was counseled on smoking cessation before his proposed surgical treatment, and for at least a year post-op to allow for the prosthetic 3-D printed implant to incorporate with the adjacent bones.

The staged approach was to first remove the locked nail that failed to fuse the ankle joint. This would be followed by implanting an antibiotic cement spacer, taking gap measurements of this stiff multiply operated ankle/foot.

"Neo Talus" implant design and implantation

The "Neo Talus" implant had to achieve not only ankle fusion, but also solid fixation with the tibia without subluxation or extrusion of the implant, fuse the subtalar joint and make sure there would not be a talo-navicular pain or subluxation with time. The design of the "neo talus" needed to have plates to the distal tibia – anteriorly and medially – and areas in its design to accommodate 2 screws fixation to each the calcaneus and the navicular. Additionally, a separate lateral plate would span from the tibia after resecting the distal fibula, cross-lateral to the "neo talus" and get affixed to the calcaneus.

In Fig. 9, AM manufactured customized implant was implanted into the excised talus space after the removal of the antibiotic cement spacer. The implant was filled with morselized bone graft obtained from the resected distal fibula (Fig. 9). The wounds were closed, and the leg and foot were immobilized in cast for a total of 6 weeks.

At 6 weeks post-op, he was transferred to a plastic molded ankle-foot orthosis (AFO) continuing non-weight bearing for 3 months. Partial weight-bearing was started, and by 5 months he was fully weight-bearing and walking with the AFO on it and no pain.

Figure 10 shows CT images of the patient's ankle 14 months after surgery. It shows the designed implant perfectly fits the bony defect area. He remained painless, walking without canes or crutches at his last follow-up at 2 years post-op.

We have good early results and a happy patient who is back to working as a surgeon using both hands, standing, and walking without the need for crutches.

We are cognizant that it is still too early to apply this approach to every case of AVN of the talus, and that there may be other ways to treat them. But in case of failures or more complicated deformed ankles and hindfeet, our solution seems to have addressed this patient's need, returning him early to gainful employment in his profession as a surgeon.
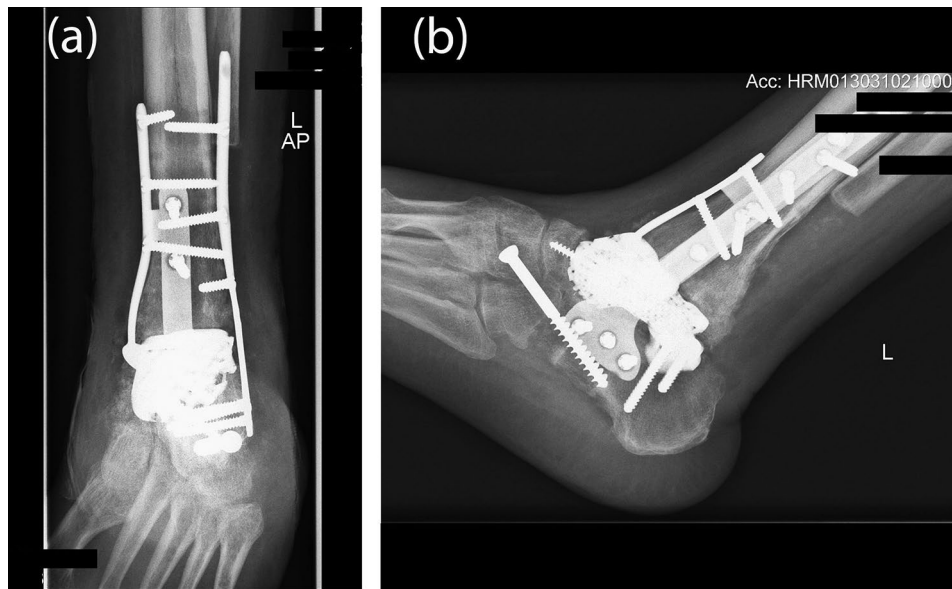
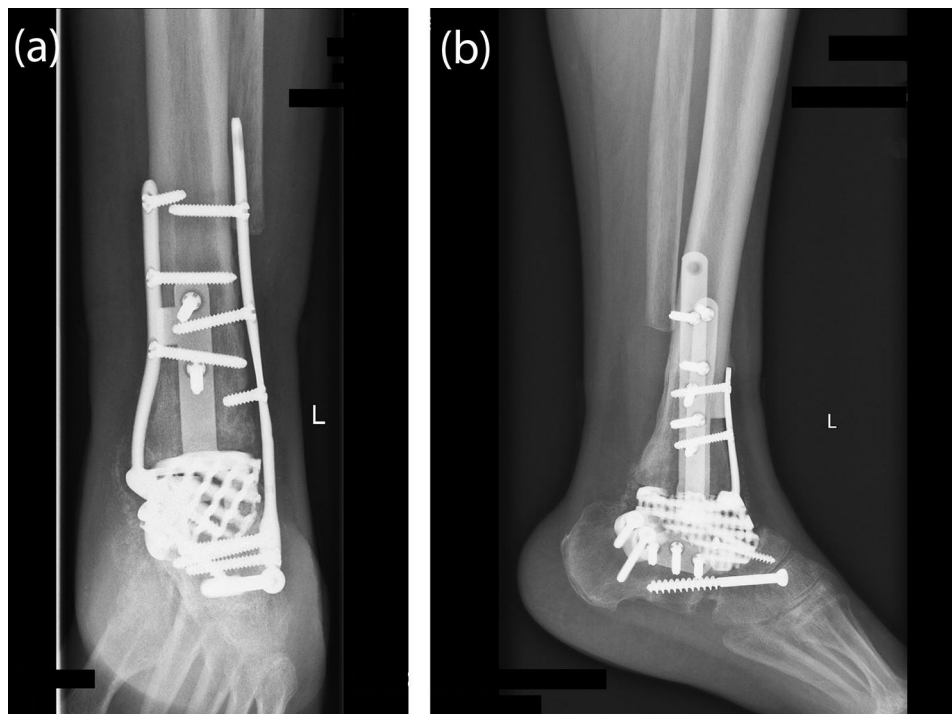**Fig. 9** X-rays after insertion of implant intra-operatively; The implant is in a correct place, (**a**) front view, (**b**) side view

Fig. 10 CT scans performed after 14 months: The implant is well aligned and in a good position (**a**) front view, (**b**) side view

Discussion

A challenge in using metallic materials for implant fabrication is the difference in stiffness between the metal and bone. This difference causes stress shielding, where the mechanical protection of the bone results in its weakening and degradation, leading to implant failure [30]. To avoid stress shielding, porous or latice structured metal materials were proposed and successfully utilized. These materials allow for fine-tuning of the topological configuration and relative density to adjust both the mechanical properties and biological functions [31–33].

Dekker et al. [16] used lattice structured 3D printed implant. They observed bone incorporation in 13 out of 15 patients, with no evidence of stress shielding or implant failure. Moreover, they resulted in significant improvements in functional outcome scores and a high

overall rate of patient satisfaction. The group extended their study including 39 cases [17]. Ten of 3D printed implants were removed because of nonunion. In the removed implants the authors noticed extensive osteo-integration. Ramhamadany et al. [18] proposed that 3D-printed lattice structured titanium implants have roughened surface which promote bone ingrowth and could prevent infection. Extensive studies have reported that a micro-/nanostructured material surface has a key role on cellular response including cell adhesion, extension, proliferation, and differentiation [34–36]. Generally, macropores ranging from 100 to 1000 μm facilitates the ingrowth of bone tissue and blood vessels, and interconnected pores ranging from 10 to 100 μm are beneficial for nutrient transport. Micropores less than 10 μm promotes protein adsorption and cell attachment [37, 38].

As addressed above, successful implantation and bone regeneration is strongly depended on several factors including shape, size, composition, etc. Therefore, in the lattice implant design, biocompatibility considerations and surface morphology all contribute to the overall success of implantation and bone regeneration. All these factors were incorporated into the implant's design and fabrication process to ensure both mechanical stability and biological integration.

Conclusion

A mesh structure of the implant was proposed and designed to reduce the weight of the implant and promote osteoconductivity.

"Rotating cross" and "Rhombic Dodecahedron" unit cells were selected to evaluate the mechanical reliability. The simulations showed that the principal stresses are concentrated at the connections of the struts. Although the stress was less than the yield strength of the structural alloy, it was estimated that the specimen could fail mechanically under dynamic loading. Increasing the strut thickness to over 1.9 mm provided a reliable structure capable of passing all tests including static and dynamic loads.

The best-estimated structure was the "rhombic dodecahedron" structure, which was able to withstand both normal and shear loads.

After pre-operational preparation and the successful operation, the implant was successfully integrated with the bone and after 14 months the X-ray image showed bone ingrowth into a mesh structure.

Supplementary Information

The online version contains supplementary material available at https://doi.org/10.1186/s13018-024-04948-w.

Supplementary Material 1

Author contributions
François Antounian contributed to the development, treatment plan and concept of design of the "Neo Talus" implant. Hayk Avagyan the patient's surgeon participated in, and reviewed the design of the implant and performed the surgery with mentorship from François Antounian.Yaroslav Holovenko participated in designing and modeling of the "Neo Talus" implant. Hayk Khachatryan made simulations. Tsovinar Ghaltaghchyan did mechanical testing and manufacturing of the implant. Marina Aghayan organized and oversaw the complete process. Marina Aghayan and Hayk Khachatryan analyzed the results and wrote the article.

Data availability
No datasets were generated or analysed during the current study.

Declarations

Competing interests
The authors declare no competing interests.

References

1. Ando Y, Yasui T, Isawa K, Tanaka S, Tanaka Y, Takakura Y. Total Talar replacement for idiopathic necrosis of the Talus: a Case Report. J Foot Ankle Surg. 2016 Nov-Dec;55(6):1292–6. https://doi.org/10.1053/j.jfas.2015.07.015. Epub 2015 Sep 18. PMID: 26387058.
2. Harnroongroj T, Harnroongroj T. The Talar Body Prosthesis: Results at Ten to Thirty-six Years of Follow-up. J Bone Joint Surg Am. 2014;96(14):1211–1218. https://doi.org/10.2106/JBJS.M.00377. PMID: 25031376.
3. Lim HK, Ryu M, Woo SH, Song IS, Choi YJ, Lee UL. Bone conduction capacity of highly porous 3D-Printed Titanium scaffolds based on different pore designs. Mater (Basel). 2021;14(14):3892. https://doi.org/10.3390/ma14143892. PMID: 34300810; PMCID: PMC8303426.
4. Meng M, Wang J, Huang H, Liu X, Zhang J, Li Z. 3D printing metal implants in orthopedic surgery: methods, applications and future prospects. J Orthop Translat. 2023;42:94–112. PMID: 37675040; PMCID: PMC10480061.
5. Salmi M, Paloheimo KS, Tuomi J, Wolff J, Mäkitie A. Accuracy of medical models made by additive manufacturing (rapid manufacturing). J Craniomaxillofac Surg. 2013;41(7):603–9. https://doi.org/10.1016/j.jcms.2012.11.041. Epub 2013 Jan 18. PMID: 23333490.
6. Johnson LG, Anastasio AT, Fletcher AN, Hendren S, Adams SB Jr. Outcomes following total Talus replacement: a systematic review. Foot Ankle Orthop. 2022;7(4):2473011421S00711. https://doi.org/10.1177/2473011421S00711. PMCID: PMC9666841.
7. Das M, Alam R, Das M, Biswal B, Samal BP, Patnaik A, Kumar Panda S, Owuor PS, Patra P, Tiwary CS. Management of hard tissue abnormalities and digital orthopaedics using additive manufacturing techniques. Oxf Open Mater Sci. 2022;2(1):itac009. https://doi.org/10.1093/oxfmat/itac009.
8. Jennison T, Dalgleish J, Sharpe I, Davies M, Goldberg A. Total talus replacements. Foot Ankle Orthop. 2023;8(1):24730114221151068. https://doi.org/10.1177/24730114221151068. PMID: 36741680; PMCID: PMC9893085.
9. Morita S, Taniguchi A, Miyamoto T, Kurokawa H, Tanaka Y. Application of a Customized Total Talar Prosthesis for Revision Total Ankle Arthroplasty. JB JS Open Access. 2020;5(4):e20.00034. https://doi.org/10.2106/JBJS.OA.20.00034. PMID: 33283130; PMCID: PMC7593043.

10. Tracey J, Arora D, Gross CE, Parekh SG. Custom 3D-Printed total Talar Prostheses restore normal joint anatomy throughout the Hindfoot. Foot Ankle Spec. 2019;12(1):39–48. Epub 2018 Mar 14. PMID: 29537314.

11. Abramson M, Hilton T, Hosking K, Campbell N, Dey R, McCollum G. Total talar replacements short-medium term Case Series, South Africa 2019. J Foot Ankle Surg. 2021 Jan-Feb;60(1):182–6. https://doi.org/10.1053/j.jfas.2020.08.015. Epub 2020 Aug 15. PMID: 33218865.

12. Hussain RM, Foot Ankle J. Surg. 2021 May-Jun;60(3):634–41. https://doi.org/10.1053/j.jfas.2020.10.005. Epub 2020 Oct 9. PMID: 33509721.

13. Morita S, Taniguchi A, Miyamoto T, Kurokawa H, Takakura Y, Takakura Y, Tanaka Y. The long-term clinical results of total Talar replacement at 10 years or more after surgery. J Bone Joint Surg Am. 2022;104(9):790–5. Epub 2022 Feb 21. PMID: 35188906.

14. Katsui R, Takakura Y, Taniguchi A, Tanaka Y. Ceramic Artificial Talus as the Initial Treatment for Comminuted Talar Fractures. Foot Ankle Int. 2020;41(1):79–83. Epub 2019 Sep 27. PMID: 31559851.

15. Kadakia RJ, Akoh CC, Chen J, Sharma A, Parekh SG. 3D printed total Talus replacement for avascular necrosis of the Talus. Foot Ankle Int. 2020;41(12):1529–36. Epub 2020 Aug 18. PMID: 32806936.

16. Dekker TJ, Steele JR, Federer AE, Hamid KS, Adams SB Jr. Use of patient-specific 3D-Printed Titanium implants for Complex Foot and Ankle Limb Salvage, deformity correction, and arthrodesis procedures. Foot Ankle Int. 2018;39(8):916–21. Epub 2018 Apr 12. PMID: 29648876.

17. Abar B, Kwon N, Allen NB, Lau T, Johnson LG, Gall K, Adams SB. Outcomes of Surgical Reconstruction using custom 3D-Printed porous Titanium implants for critical-sized bone defects of the Foot and Ankle. Foot Ankle Int. 2022;43(6):750–61. Epub 2022 Feb 24. PMID: 35209733; PMCID: PMC9177519.

18. Ramhamadany E, Chadwick C, Davies MB. Treatment of severe avascular necrosis of the Talus using a Novel keystone-shaped 3D-Printed Titanium Truss Implant. Foot Ankle Orthop. 2021;6(4):24730114211043516. https://doi.org/10.1177/24730114211043516. PMID: 35097475; PMCID: PMC8554568.

19. Pei X, Wu L, Zhou C, Fan H, Gou M, Li Z, Zhang B, Lei H, Sun H, Liang J, Jiang Q, Fan Y, Zhang X. 3D printed titanium scaffolds with homogeneous diamond-like structures mimicking that of the osteocyte microenvironment and its bone regeneration study. Biofabrication. 2020;13(1). https://doi.org/10.1088/1758-5090/abc060. Erratum in: Biofabrication. 2021;13(3). doi: 10.1088/1758-5090/abdb89. PMID: 33045688.

20. Ghorbani F, Li D, Ni S, Zhou Y, Yu B. 3D printing of acellular scaffolds for bone defect regeneration: a review. Mater Today Commun. 2020;22. https://doi.org/10.1016/j.mtcomm.2020.100979.

21. Wubneh A, Tsekoura EK, Ayranci C, Uludağ H. Current state of fabrication technologies and materials for bone tissue engineering. Acta Biomater. 2018;80:1–30. https://doi.org/10.1016/j.actbio.2018.09.031. Epub 2018 Sep 22. PMID: 30248515.

22. Ko SY, Hong JY, Lee W, Chang YY, Park KB, Yun JH. Osteoconductivity of Porous Titanium structure on implants in osteoporosis. J Dent Res. 2021;100(10):1178–85. Epub 2021 Jul 8. PMID: 34235985.

23. Jiao J, Hong Q, Zhang D, Wang M, Tang H, Yang J, Qu X, Yue B. Influence of porosity on osteogenesis, bone growth and osteointegration in trabecular tantalum scaffolds fabricated by additive manufacturing. Front Bioeng Biotechnol. 2023;11:1117954. https://doi.org/10.3389/fbioe.2023.1117954. PMID: 36777251; PMCID: PMC9911888.

24. Dallago M, Raghavendra S, Luchin V, Zappini G, Pasini D, Benedetti M. The role of node fillet, unit-cell size and strut orientation on the fatigue strength of ti-6al-4v lattice materials additively manufactured via laser powder bed fusion. Int J Fatigue. 2021;142:105946. https://doi.org/10.1016/j.ijfatigue.2020.105946.

25. Han L, Che S. An overview of materials with triply periodic minimal surfaces and related geometry: from biological structures to self-assembled systems. Adv Mater. 2018;30(17):1705708. https://doi.org/10.1002/adma.201705708.

26. Mirzaali MJ, Azarniya A, Sovizi S, Zhou J, Zadpoor AA. 16 - lattice structures made by laser powder bed fusion. In: Yadroitsev I, Yadroitsava I, du Plessis A, MacDonald E, editors. Fundamentals of Laser Powder Bed Fusion of metals. Additive Manufacturing Materials and Technologies Elsevier; 2021. pp. 423–65.

27. Zhang C, Zhang L, Liu L, Lv L, Gao L, Liu N, Wang X, Ye J. Mechanical behavior of a titanium alloy scaffold mimicking trabecular structure. J Orthop Surg Res. 2020;15(1):40. https://doi.org/10.1186/s13018-019-1489-y. PMID: 32028970; PMCID: PMC7006186.

28. Khasian M, Meccia BA, LaCour MT, Komistek RD. A validated Forward Solution Dynamics Mathematical Model of the knee Joint: can it be an Effective Alternative for Implant evaluation? J Arthroplasty. 2020;35(11):3289–99. https://doi.org/10.1016/j.arth.2020.06.017. Epub 2020 Jun 14. PMID: 32631725.

29. Wojnicz W, Augustyniak M, Borzyszkowski P. Mathematical approach to design 3D scaffolds for the 3D printable bone implant. Biocybernetics Biomedical Eng. 2021;41(2):667–78. https://doi.org/10.1016/j.bbe.2021.05.001.

30. Huiskes R, Weinans H, van Rietbergen B. The relationship between stress shielding and bone resorption around total hip stems and the effects of flexible materials. Clin Orthop Relat Res. 1992;(274):124–34. PMID: 1728998.

31. Bobbert FSL, Lietaert K, Eftekhari AA, Pouran B, Ahmadi SM, Weinans H, Zadpoor AA. Additively manufactured metallic porous biomaterials based on minimal surfaces: a unique combination of topological, mechanical, and mass transport properties. Acta Biomater. 2017;53:572–84. https://doi.org/10.1016/j.actbio.2017.02.024.

32. Yi B, Xu Q, Liu W. An overview of substrate stiffness guided cellular response and its applications in tissue regeneration. Bioact Mater. 2021;15:82–102. https://doi.org/10.1016/j.bioactmat.2021.12.005. PMID: 35386347; PMCID: PMC8940767.

33. Plessis A, Mohammad S, Razavi J, Benedetti M, Murchio S, Leary M, Watson M, Bhate D, Berto F. Properties and applications of additively manufactured metallic cellular materials: a review. Prog Mater Sci. 2022;125. https://doi.org/10.1016/j.pmatsci.2021.100918.

34. Tawfick S, De Volder M, Copic D, Park SJ, Oliver CR, Polsen ES, Roberts MJ, Hart AJ. Engineering of micro- and nanostructured surfaces with anisotropic geometries and properties. Adv Mater. 2012;24(13):1628–74. https://doi.org/10.1002/adma.201103796. Epub 2012 Mar 6. PMID: 22396318.

35. Urist MR. Bone: formation by autoinduction. Science. 1965;150(3698):893-9. https://doi.org/10.1126/science.150.3698.893. PMID: 5319761.

36. Ozdemir T, Higgins AM, Brown JL. Osteoinductive biomaterial geometries for bone regenerative engineering. Curr Pharm Des. 2013;19(19):3446-55. https://doi.org/10.2174/1381612811319190010. PMID: 23432675.

37. Wang J, Chen Y, Zhu X, Yuan T, Tan Y, Fan Y, Zhang X. Effect of phase composition on protein adsorption and osteoinduction of porous calcium phosphate ceramics in mice. J Biomed Mater Res A. 2014;102(12):4234–43. https://doi.org/10.1002/jbm.a.35102. Epub 2014 Feb 11. PMID: 24497384.

38. Chen H, Wang C, Zhu X, Zhang K, Fan Y, Zhang X. Fabrication of porous titanium scaffolds by stack sintering of microporous titanium spheres produced with centrifugal granulation technology. Mater Sci Eng C Mater Biol Appl. 2014;43:182-8. https://doi.org/10.1016/j.msec.2014.07.026. Epub 2014 Jul 11. PMID: 25175203.

Publisher's Note